Acta Materialia 272 (2024) 119956

Contents lists available at ScienceDirect

Acta Materialia

journal homepage: www.elsevier.com/locate/actamat

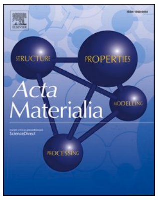

Anomalous magnetization induced by local chemistry fluctuations in Mn-containing α’-martensite

Maria J.R. Sandim [a,*], Luiz C.C.M. Nagamine [b], Alisson Kwiatkowski da Silva [c], Leonardo S. Aota [c], Liuliu Han [c], Renato Cohen [b], Hugo R.Z. Sandim [a], Baptiste Gault [c], Isnaldi R. Souza Filho [c,d]

[a] *Lorena School of Engineering, University of Sao Paulo, 12602-810, Lorena, SP, Brazil*
[b] *Institut of Physics, University of Sao Paulo, 05508-090, Sao Paulo, SP, Brazil*
[c] *Max-Planck-Institut für Eisenforschung, MPIE, D-40237 Düsseldorf, Germany*
[d] *Institut Jean Lamour, CNRS (UMR 7198), Université de Lorraine, F-54000, Nancy, France*

ARTICLE INFO

Keywords:
High-Mn TRIP steel
Anomalous magnetization
Villari effect
Short-range solute redistribution
Long-range chemical partitioning

ABSTRACT

An anomalous increase in magnetization was investigated in a cold-rolled high-Mn TRIP steel (16.8 wt% Mn) annealed at 350°C for times varying from 5 to 120 min, before the start of austenite reversion (α’ → γ). Besides in-situ and ex-situ magnetic measurements, the full characterization of this phenomenon was also performed with the aid of X-ray diffraction (XRD), Mössbauer spectroscopy, and microstructural characterization using electron backscatter diffraction (EBSD) and atom probe tomography (APT). Based on XRD measurements, the volume fraction of austenite and α’-martensite was estimated as a function of annealing time, as well as their lattice strain. Phase quantification confirmed the absence of newly-fresh α’-martensite in the material during annealing at 350°C. Short annealing up to 15 min promoted the increase of M_s (saturation magnetization) due to stress relief in α’-martensite (Villari effect). Further annealing to 30 min promotes the decrease in M_s driven by short-range solute reorganization within the lattice. After 60 min annealing, the creation of long-range solute-depleted zones (i.e. confined zones highly enriched in Fe) causes a new increase in M_s. In comparison, for 120 min of annealing time, M_s tends to remain unaltered. These findings revealed that short- and long-range chemical fluctuations strongly affect the saturation magnetization of the steel and brought new insights on the use of magnetic probing as a tool for phase quantification in Mn-bearing steels.

1. Introduction

Metallurgical reactions, i.e., phase transformations, are known to play a critical impact on the coercivity and Curie temperature of a wide range of magnetic materials, including Alnico magnets [1], Cu-Fe-Ni [2,3] and Fe-Cr-Co [4] ternary systems, and Al-Mn binary ferromagnetic alloys [5]. However, some metallurgical changes in systems presenting the transformation-induced plasticity (TRIP) effect, and their influence on the magnetization have not yet been precisely sorted out. TRIP transforms the paramagnetic fcc austenitic matrix (γ) into the bcc ferromagnetic α’-martensite upon straining [6]. Depending on the stacking fault energy (SFE) of the alloy, and on the imposed strain rates, the γ → α’ transformation can proceed with the intermediate presence of the hcp ε- martensite (i.e., γ → ε → α’), which is also a paramagnetic phase [7–12].

Many scientific aspects remain unclear when considering how both, the internal stresses [13–15] and local chemical changes within α’-martensite, impact the magnetic properties of steels. For example, an “anomalous” increase in magnetization has been reported in both austenitic and lean duplex steels with regions partially transformed into α’-martensite and aged at low temperatures of about 400°C, immediately before the start of austenite reversion (α’ → γ) [16–23]. Over decades, this behavior was controversially suggested to be caused by an ‘anomalous’ increase in the volume fraction of α’-martensite. The apparent coalescence of the α’-phase was suggested to be enabled through stress relief inside the adjacent austenite grains, permitting α’-martensite to get unconstrained. Another possible explanation was given by the formation of carbides at austenite grain boundaries which leads to the formation of C-depleted regions with higher martensitic starting temperature ($M_s^{\alpha'}$). Thus, under cooling these regions are more

---

* Corresponding author.
E-mail address: msandim@usp.br (M.J.R. Sandim).

https://doi.org/10.1016/j.actamat.2024.119956
Received 21 August 2023; Received in revised form 24 March 2024; Accepted 23 April 2024

susceptible to transform into α'-martensite, slightly increasing its volume fraction [17,24]. However, short-range solute rearrangement, elemental segregation, and the magnitude of the stress state within the α'-martensite have not yet been addressed as possible metallurgical mechanisms responsible for the anomalous magnetization.

In preceding studies, we have investigated the TRIP effect as well as the austenite reversion in a cold-rolled high-Mn TRIP steel (17.3 wt% Mn) [25,26]. For a true (logarithmic) strain $\varepsilon = 1.56$ and under annealing at ~350°C (just before the α' → γ transformation), this material showed a slight increase in its magnetization, alluding to the anomalous magnetization. For such a deformation level, this material is almost fully composed of α'-martensite (~ 99 vol.%). The remaining 1 vol.% of the material was occupied by retained ε-phase [25]. Therefore, the 'anomalous increase in α'-content' driven by stress relaxation in surrounding austenite seems not to be an adequate hypothesis in the present study. Besides, the possible precipitation of $M_{23}C_6$ was inferred to occur in the α'-phase rather than in austenite in this steel [26]. In light of this observations, the aim of this work is to elucidate the raise in magnetization at 350 °C and understand the corresponding underlying mechanisms, based on the influence of internal stresses, short- and long-range chemical fluctuations on the magnetic properties of high-Mn steels. With this goal, we monitored the magnetization of the steel under in-situ and ex-situ annealing conditions. The corresponding metallurgical reactions were tracked by several probes, including Mössbauer spectroscopy, high resolution X-ray diffraction (XRD) measurements, electron backscatter diffraction (EBSD) and near-atomic resolution atom probe tomography (APT). Conversely to reports in Refs. [16–20], our findings reveal that annealing at low temperatures trigger stress relief, short- and long-range chemical partitioning within the α'-martensite. These reactions lead to the creation of new chemical configurations in the lattice during short annealing times and submicron-sized zones enriched in iron after longer annealing periods. With this work, we aim to bring new perspectives on how metallurgical changes in the α'-martensite direct contribute to the bulk 'anomalous' magnetization in a high-Mn TRIP steel.

2. Experimental

2.1. Material

The steel studied in this work is a high-Mn TRIP steel whose chemical composition is displayed in Table 1. The steel in the as-received condition (7-mm-thick) was cold rolled to 20 % and 80 % of thickness reduction in multiple passes, as reported in preceding studies [25,26]. It is important to mention that this steel is similar but not the same one investigated in references [25,26].

2.2. Magnetic measurements

For magnetic measurements, specimens with dimensions of approximately $6 \times 2 \times 1$ and $6 \times 1 \times 1\ \mathrm{mm}^3$ were cut from the 20 and 80 % cold-rolled plates, respectively. The largest dimension (6 mm) was taken parallel to the rolling direction (RD) of the plate. In-situ magnetic measurements were carried out during continuous annealing. For this set of experiments, one specimen obtained from the plate deformed to 80 % was continuously annealed from room temperature to 450°C with a heating rate of 0.05 °C/s in the presence of an external magnetic field of ~90 Oe. This experiment was conducted under high-purity argon flow (99.999 %) using a vibrating-sample magnetometer (VSM) Lake Shore model 7404.

Table 1
Chemical composition of the high-Mn TRIP steel studied in this work, given in both at. and wt. %.

	Mn	Al	Si	C	Ni	Fe
wt.%	16.8	1.55	1.88	0.01	1.17	Bal.
at.%	16.5	3.10	3.60	0.045	1.07	Bal.

Specimens obtained from the steel deformed to 20 and 80 % were isothermally annealed at 350°C during time periods ranging from 5 to 120 min and air cooled. After cooling, hysteresis loops (ex-situ magnetic measurements) were acquired for each sample at room temperature using a VSM from EG&G Princeton Applied Research. In all magnetic experiments, the external magnetic field was applied parallel to the largest dimension of the specimen (6 mm), i.e., parallel to the RD. Coercive field (H_c) and saturation magnetization (M_s) were obtained from the hysteresis loops with an accuracy of ±5 Oe and 2 % of the measured value, respectively.

2.3. X-ray diffraction (XRD) measurements

The specimens obtained from the steel deformed to 20 % and isothermally annealed at 350 °C (5-120 min) were submitted to high-resolution XRD measurements after being used for the acquisition of the hysteresis loops as described in Section 2.2. For each sample, the surface perpendicular to the transverse direction (TD) of the plate was ground and polished with colloidal silica suspension. High-resolution XRD measurements were conducted using a Bruker D8-MU diffractometer with cobalt radiation ($\lambda = 0.178897$ nm) operated at 40 kV and 40 mA. Due to the relative low level of straining imposed by 20 % of rolling reduction, we expect a minor influence of crystallographic texture on peak intensities. Nevertheless, to minimize any influence arising from texture, the 1-mm-diameter beam was positioned in the mid-length of the specimen (3 mm) and the experiments were conducted under wobbling with an amplitude of 1 mm. Besides, the statistics of data acquisition were enhanced by using a Vantec 500 2D detector. The instrumental contribution of the equipment was determined by reproducing the same conditions of measurement for a standard high-purity silicon sample.

The diffraction data were converted into usual plots of intensity versus the diffraction angles (2θ) within the interval between 43 and 105°. The experimental data was fitted by a pseudo-Voigt function to assess information regarding peak position, corresponding integrated intensity and the values of full width at half maximum (FWHM). Phase quantification was conducted by subjecting the fitted data to the direct peak intensity comparison method as outlined in Refs [27–30], where the integrated intensity of the peaks belonging to a certain phase is considered to be proportional to its volume fraction in the specimen. The modified Williamson-Hall method [31,32] was used to assess the lattice strain ($\varepsilon_{\text{lattice}}$) in austenite and α'-martensite using

$$\frac{2(\mathrm{FWHM})\cos\theta}{\lambda} \cong \frac{1}{D} + \varepsilon_{lattice}\cdot\left[\left(\frac{2\sin\theta}{\lambda}\right)^2\cdot\overline{C}_{h00}\cdot\left(1-qH^2\right)\right] \tag{1}$$

where $\varepsilon_{\text{lattice}}$ is the magnitude of the lattice strain, D is the size of the coherent domains (crystallites) responsible for scattering X-rays, and $\overline{C}_{h00}$ is a parameter associated to the elastic constants of the material [31,32]. H^2 is defined as being $(h^2k^2 + h^2l^2 + k^2l^2)/(h+k+l)^2$ and q stands for the character of the dislocations [31,32]. Here, $\overline{C}_{h00}$ is assumed as 0.332 and 0.285 for austenite and α'-martensite, respectively [27–29]. For a certain phase, the values of D and $\varepsilon_{\text{lattice}}$ were determined by keeping the term $\left(\frac{2\sin\theta}{\lambda}\right)^2\cdot\overline{C}_{h00}\cdot(1-qH^2)$ as a linear function of $\frac{2(\mathrm{FWHM})\cos\theta}{\lambda}$. To achieve the linearity, the values of q were taken as those which provided the best linear fit for Eq. (1).

2.4. Microstructural characterization

Representative samples were metallographic prepared for microstructural characterization via electron backscatter diffraction (EBSD) mappings. High-resolution EBSD maps were acquired using a step size of 50 nm using an EDAX Hikari system coupled to a JEOL-6500F field-emission scanning electron microscope (SEM). Confidence index (CI) standardization protocol was adopted as a cleanup procedure and all pixels with CI below 0.1 were removed from the maps.

2.5. Mössbauer transmission measurements

Mössbauer spectroscopy (MS) transmission geometry measurements were performed using a 50 mCi ^{57}Co/Rh source and a constant-acceleration drive using a triangular-shaped wave form. The drive velocity was calibrated with a α-Fe foil. Both Mössbauer source and sample were kept at room temperature. Samples were prepared as foils with 20 and 40 μm in thickness from the steel deformed to 80 % and from the corresponding plate annealed at 350 °C for 30 min, respectively. The surface of both specimens was parallel to the rolling plane.

2.6. Atom probe tomography (APT)

APT measurements were conducted for samples obtained from the steel deformed to 80 % and subsequently annealed at 350 °C for 60 and 120 min. Needle-shape specimens were prepared for APT using a FEI Helios 600i dual-beam focused ion beam milling/scanning electron microscope (FIB-SEM). For extraction of the specimens, the FIB lift-out method was adopted as outlined in Ref. [33]. All specimens were mounted on Si micro-tips and sharpened by annular ion milling. APT was performed on a LEAP 5000 XS straight flight path instrument at 60 K in laser-pulse mode operated at 40 pJ pulse energy. The wavelength, pulse and detection rates of the laser were 355 nm, 500 kHz and 1.5 ions detected on average per 100 pulses, respectively. Data reconstruction and analysis were employed using the Cameca IVAS® software following the protocol reported by Geiser et. al [34].

2.7. Thermodynamic calculations

Based on the chemical composition of the steel (Table 1), stability of the phases in thermodynamic equilibrium was calculated using ThermoCalc with the aid of the database TCFE9.

3. Results

3.1. Microstructural evolution upon cold rolling

The EBSD phase maps displayed in Fig. 1a show that the initial microstructure of the high-Mn TRIP steel consists of equiaxed austenite grains partially subdivided by traces of athermally formed ε- and α’-martensite. The steel was cold rolled down to 20 % (Fig. 1b) and 80 % (Fig. 1c) reduction to obtain microstructures with different volume fractions of strain-induced α’-martensite. For this material, both the athermally-formed and strain-induced α’-domains are primarily found within the ε-martensite platelets. The volume fractions of austenite, ε- and α’-martensite at 20 % reduction were estimated from Fig. 1b as being 0.44, 0.20, and 0.36, respectively. The steel deformed to 80 % is majorly composed of α’-martensite (volume fraction of approximately 0.99). No traces of untransformed austenite were detected in the EBSD analysis displayed in Fig. 1c and a residual fraction of 0.01 of ε-domains remains untransformed into α’-martensite after 80 % rolling.

3.2. In-situ magnetic measurements

The changes in magnetization (M) were tracked in-situ during annealing. The steel deformed to 80 % reduction was continuously heated to 450 °C with a heating rate of 0.05 °C/s, under a constant external magnetic field (H) of 90 Oe (Section 2.2). The magnetic response of the sample during continuous annealing is reported in Fig. 2a. Fig. 2b shows the values of M within the temperature range between 310 and 400 °C. The initial drop in magnetization up to 335 °C is likely a consequence of the decreasing of the magnetocrystalline constants with increasing temperature [15,26]. However, preceding the onset of the austenite reversion ($A_s = 375$ °C), an anomalous increase in M is observed within the temperature interval between 339 and 375 °C. At this point, it is worth mentioning that the detection limit of the vibrating-sample magnetometer (VSM) used in this experiment is 10^{-4} emu (or 0.0019 emu/g, if normalized by the mass of the probed specimen). Therefore, the raise in magnetization observed in Fig. 2 can be attributed to actual microstructural modifications in the steel.

3.3. Ex-situ magnetic measurements

Based on the observed anomalous magnetization that precedes austenite reversion (Fig. 2), isothermal annealing was conducted at 350 °C for durations from 5 to 120 min for samples obtained from the steel deformed to 20 and 80 % reductions (Section 2.2). Reproducing the same annealing conditions for two distinct deformation levels obtained via cold rolling will help to understand the effects of different phase fractions on the magnetic properties. After annealing, magnetic hysteresis loops (i.e., M-H curves) were acquired at room temperature for each sample, as shown in Fig. 3a and b for the materials respectively deformed to 20 % and 80 % and annealed at 350°C for several minutes (up to 120 min).

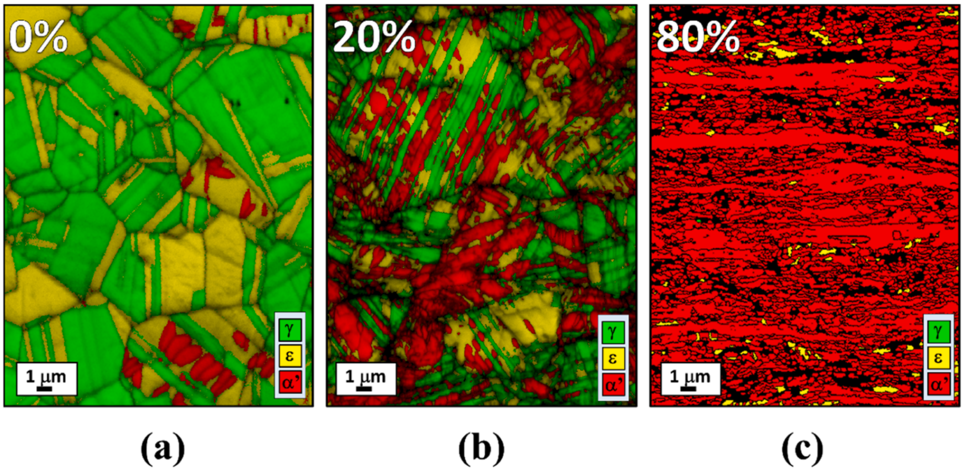

Fig. 1. EBSD microstructural analysis of the high-Mn TRIP steel in the **(a)** as-received condition and strained to **(b)** 20 % and **(c)** 80 % of rolling reduction. In these EBSD phase maps, austenite, ε- and α’-martensite are displayed in green, yellow and red, respectively. (For interpretation of the references to color in this figure legend, the reader is referred to the web version of this article.)

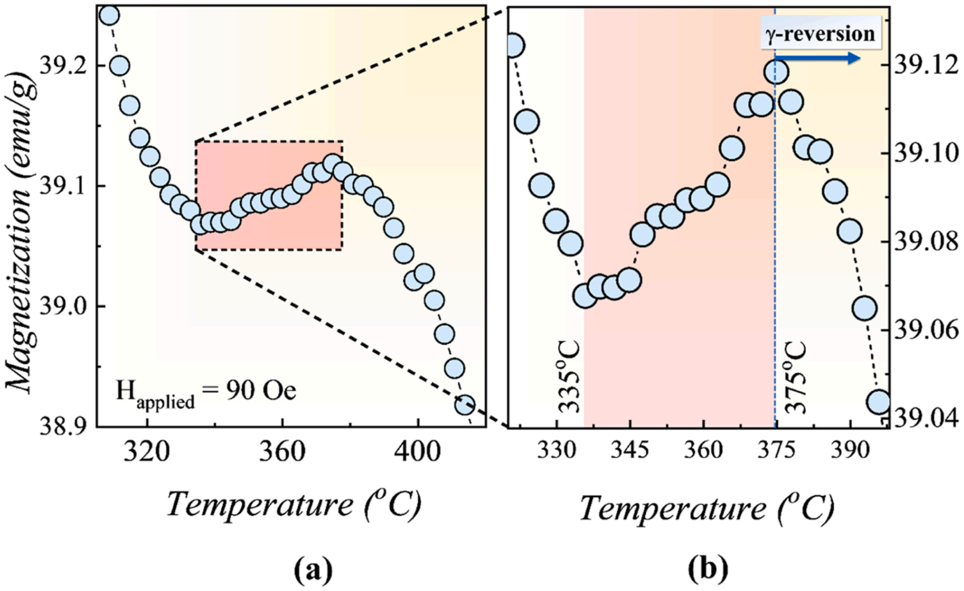

Fig. 2. (a) In-situ magnetic measurements for the steel deformed to 80 %, conducted during continuous heating (0.05 °C/s) under the presence of an external magnetic field of 90 Oe; **(b)** highlights the anomalous change in magnetization within the temperature interval between 335 and 375 °C.

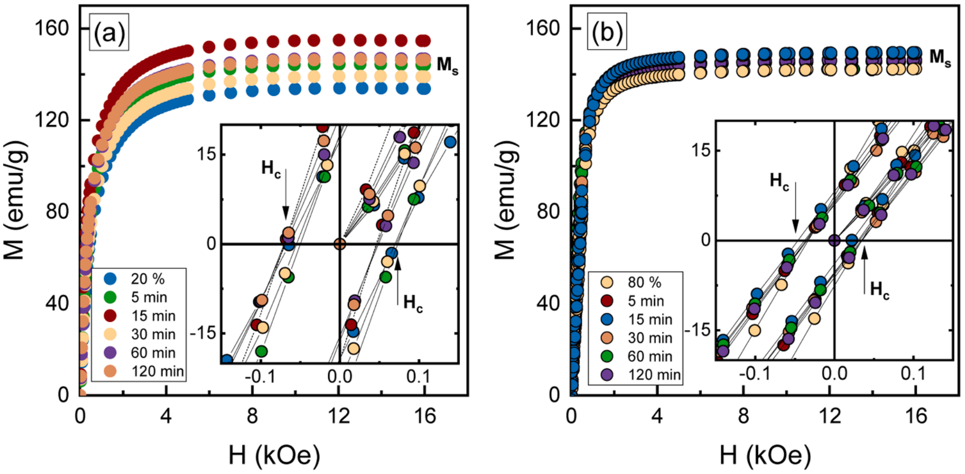

Fig. 3. Magnetization as a function of applied field (taken at room temperature) for the high-Mn TRIP steel with (a) 20 and (b) 80 % reduction, annealed at 350°C from 5 up to 120 min. The insets show the corresponding coercive fields for each of the M–H curves. (For interpretation of the references to color in this figure legend, the reader is referred to the web version of this article.)

For each M-H curve, the absolute values of magnetization were normalized by the corresponding mass of α′-martensite contained in the probed sample, the latter was determined as documented in the Supplementary Material. For the sake of simplicity, the normalized magnetization values obtained for $H < 0$ are not show in Fig. 3. The insets of Fig. 3 highlight the positive (+) and negative (-) coercive field (H_c) variants of each sample. The data displayed in Fig. 3 is indispensable to provide us with the corresponding values of the saturation magnetization (M_s) – for this parameter, please, see additional information in the Supplementary Material – and the coercive field (H_c), calculated as the average between the absolute H_c variants. The changes in M_s and H_c as a function of the annealing time (t) are shown in Fig. 4a and b, respectively.

Fig. 4a shows that the magnitude of straining seems to exert a minor influence on the overall shape of both “M_s *versus* t” curves, allowing to distinguish the four distinct stages indicated in Fig. 4a. During stage 1, M_s increases with 5 min of annealing and remains nearly unchanged after 15 min. During stage 2, M_s drops in approximately 4 emu/g in both conditions but raises again until reaching a maximum peak value in 60 min comprising the stage 3. The stage 4, in turn, shows an apparent further slight drop in the absolute value of M_s with 120 min of annealing. However, a more careful inspection reveals that such drop is within the inaccuracy range (the inaccuracy values of our ex-situ magnetic experiments correspond to 2 % of the absolute M_s value). Thus, over the course of stage 4, we can infer that M_s remains nearly unchanged. Conversely, the coercivity of the steel deformed at both 20 and 80 % reduction levels remains nearly unchanged over the entire annealing range (Fig. 4b). Only a slight relaxation after 5-min annealing was detected in the material deformed to 80 % reduction, as a likely consequence of static recovery in α’-martensite.

3.4. XRD analysis

Due to the similar trend of both “M_s *versus* t” curves displayed in Fig. 4a, high-resolution XRD measurements were employed only for the specimens obtained from the steel deformed to 20 % and isothermally

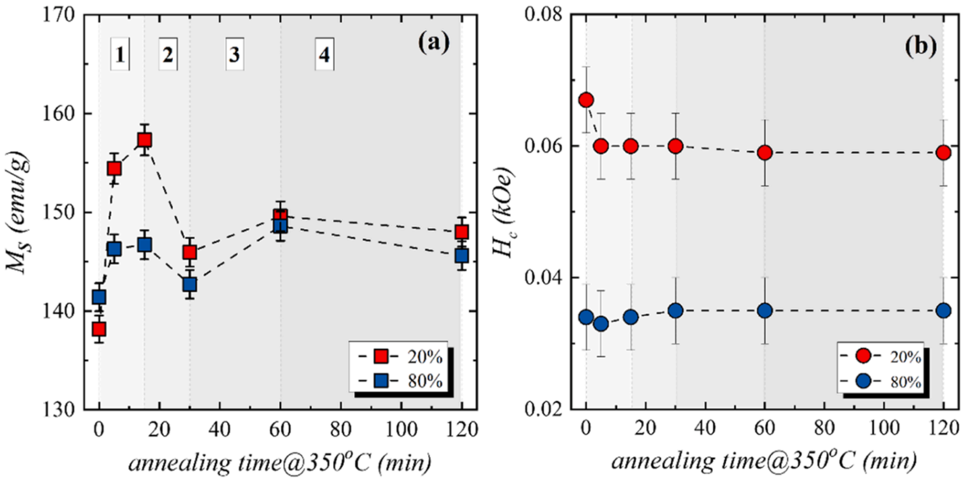

Fig. 4. Changes in the **(a)** saturation magnetization and in the **(b)** coercive field as a function of annealing time at 350 °C for both rolling reductions. (For interpretation of the references to color in this figure legend, the reader is referred to the web version of this article.)

annealed at 350 °C. Fig. 5a shows part of the corresponding diffractograms for which we applied the peak intensity comparison method [27–29] to assess the volume fraction ($f_{vol.}$) of the phases, as displayed in Fig. 5b. The error bars shown in Fig. 5b stands for a phase fraction of 0.03 which corresponds to the limit of detection of the technique [35]. The very small peaks of ε-martensite in the annealed specimens confirm that this constituent is not completely transformed back into austenite under these annealing conditions (arrows in Fig. 5a). However, the low intensity associated to these peaks hinders the proper quantification via XRD of the ε-martensite in the annealed specimens. Fig. 5b reveals no substantial modifications in the volume fraction of the α'-martensite during annealing, whose values remain nearly constant at about 0.36.

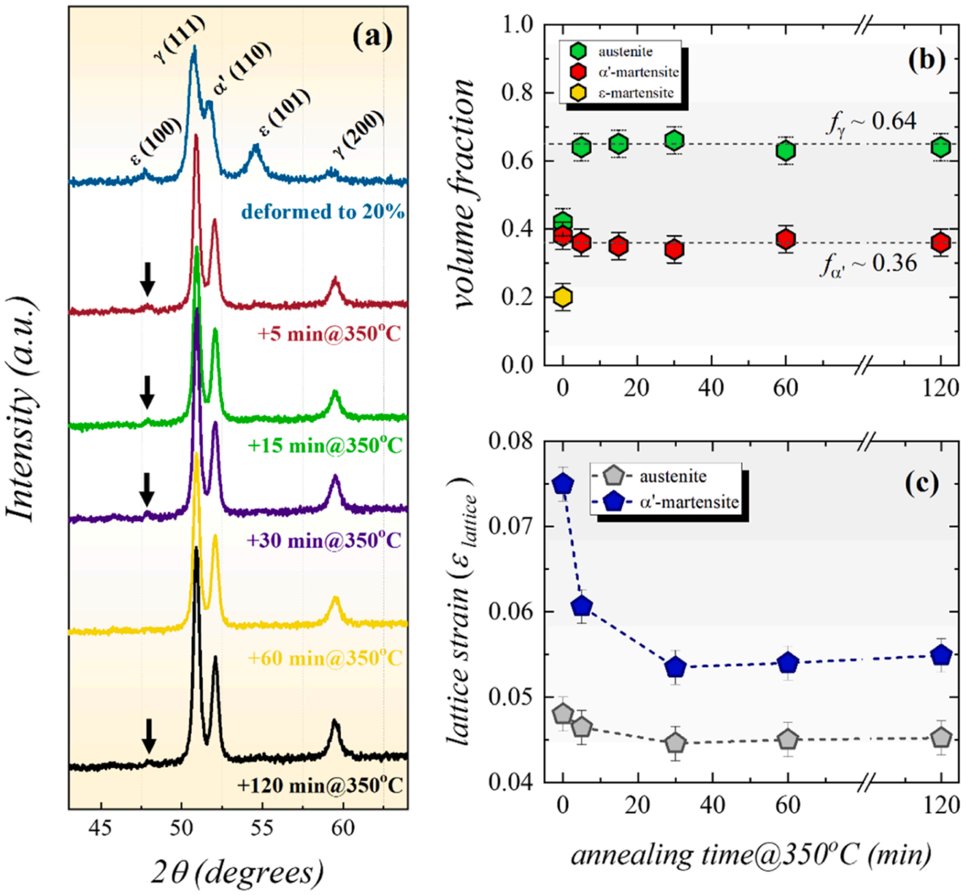

Fig. 5. **(a)** High-resolution diffractograms acquired for the steel deformed to 20 % and isothermally annealed at 350 °C for different annealing times (5–120 min). For the sake of clarity, only the interval of 2θ between 43 and 64° is shown; **(b)** Changes in the phase volume fraction during the isothermal annealing at 350 °C, obtained by applying the direct peak intensity comparison method to the diffracted data shown in (a); **(c)** Evolution of the magnitude of the lattice strain ($\varepsilon_{\text{lattice}}$) of austenite and α'-martensite during isothermal annealing at 350 °C. $\varepsilon_{\text{lattice}}$ was obtained by employing the modified Williamson–Hall plots to the data displayed in (a). (For interpretation of the references to color in this figure legend, the reader is referred to the web version of this article.)

The sharp increase of the austenite fraction after 5 min of annealing is attributed to the non-diffusional-driven $\varepsilon \rightarrow \gamma$ reaction [36].

The modified Williamson-Hall method [31,32] was applied to the diffraction data partially displayed in Fig. 5a to evaluate the magnitude of the lattice strain ($\varepsilon_{\text{lattice}}$) in austenite and α’-martensite, as reported in Fig. 5c as a function of the annealing time at 350°C. The protocol adopted to estimate the errors associated with the lattice strain is detailed in the Supplementary file. Fig. 5c reveals that the magnitude of $\varepsilon_{\text{lattice}}$ in the α’-martensite sharply drops already in the early 30 min of annealing (i.e., during stages 1 and 2), whilst the corresponding relaxation in the austenite is more discreet. This trend suggests that stress relief within the α’-martensite is higher than that in the austenite upon annealing at 350 °C.

3.5. *Microstructural evolution upon annealing*

Fig. 6 shows representative microstructures of the steel deformed to 20 % and subsequently annealed at 350 °C, assessed by means of high-resolution EBSD phase maps. In this figure, austenite, ε-, and α’-martensite are represented in green, yellow, and red, respectively. The sequential series of microstructures reported in Fig. 6 reveals no significant changes in terms of morphology for the α’-martensite grains, as well as in their volumetric fraction. Ultra-fine austenite regions can be distinguished immersed within α’-martensite, as evidenced by the dashed frames in Fig. 6. As the γ/α’ pairs are seldomly observed in the deformed state (Fig. 1b), due to the fact that ε-martensite intermediates the α’-formation in this steel, it is plausible to assume that the ultra-fine γ-regions observed in Fig. 6 replace the prior ε-martensite plates, i.e., constituting of fresh-reversed γ.

3.6. *Mössbauer spectroscopy*

Fig. 7a and b show the Mössbauer spectra taken at room temperature for the steel deformed to 80 % reduction and for the corresponding specimen annealed at 350°C during 30 min, respectively. Before

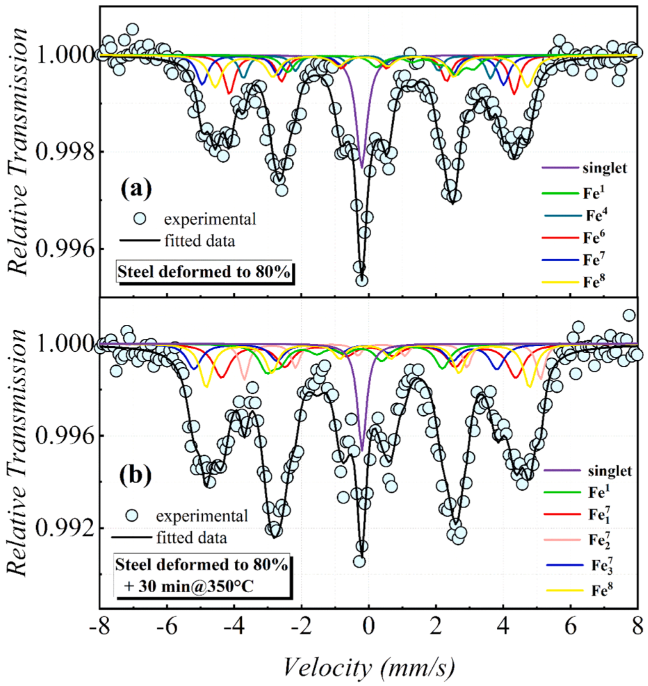

Fig. 7. Room temperature Mössbauer spectra of the specimens **(a)** deformed to 80 % of rolling reduction and **(b)** deformed to 80 % and isothermally annealed at 350 °C for 30 min. The blue circles and black line represent the experimental data and the corresponding fitting, respectively. The corresponding subspectra for the sextets (Fe^i, where “i” varies from 8 to 1) and singlets are properly identified in this figure. (For interpretation of the references to color in this figure legend, the reader is referred to the web version of this article.)

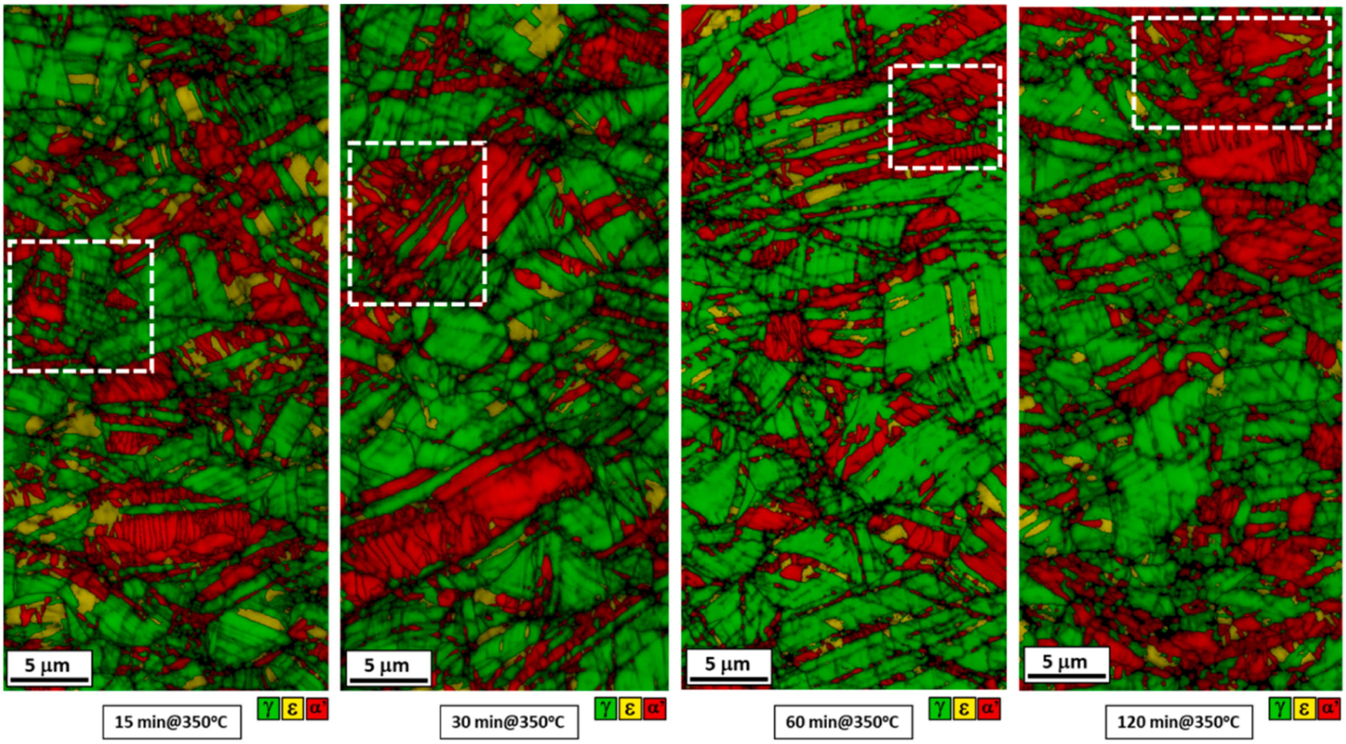

Fig. 6. Microstructural evolution of the 20 %-deformed steel annealed at 350 °C for **(a)** 15 min; **(b)** 30 min; **(c)** 60 min and **(d)** 120 min. Microstructures observed with the aid of EBSD phase maps where austenite, ε-, and α’-martensite are displayed in green, yellow and red, respectively. (For interpretation of the references to color in this figure legend, the reader is referred to the web version of this article.)

determining the chemical environment in the surroundings of the Fe-atoms via analysis of the spectra reported in Fig. 7, one must recall that each site of the bcc lattice has eight first nearest neighbors (NN). Thus, in this work, the terms "Fe^i" (where $i = 8, 7, 6, 4, 1$) will be used to indicate the sites occupied by a Fe-atom that has the number "i" of other Fe-atoms as NN.

The experimental data shown in Fig. 7 was fitted with subspectra composed of five sextets and one singlet. The sextet arises from the magnetic contribution of the α'-martensite and are labeled in Fig. 7 as Fe^8, Fe^7 (also as Fe^7_1, Fe^7_2, and Fe^7_3, as it will be explained later in Fig. 7b), Fe^6, Fe^4 and Fe^1. The singlet in turn is assigned to the paramagnetic austenite and/or ε-martensite phases and it is found at approximately −0.2 mm/s in Fig. 7. The values of hyperfine field ($B_{hf}^{Fe^i}$), isomer shift (δ), quadrupole splitting (2ε) and relative area (A^{Fe^i}) of each subspectrum were obtained via fitting of the data reported in Fig. 7 and reported in Table 2. The values of δ were calculated in relation to a spectrum of reference produced by a high-purity α-iron foil.

Table 2 shows that the relative area of singlet decrease from 15.8 to 7.2, when the specimen (80 % reduction) is annealed at 350°C. For both specimens, as the number of non-iron NNs increases from zero (i.e., Fe^8) to one (Fe^1), the magnetic hyperfine field decreases as a consequence of the decrease of the local magnetic exchange interaction of the Fe-Fe bonds (i.e. the hyperfine fields are directly related to the number of Fe first NN) [37–39]. A decreasing of 1.54 T/(non-iron NN) and 1.90 T/(non-iron NN) were obtained from the linear fits of B_{hf} versus numbers of iron-NN for the steel deformed to 80 % and annealed (30 min at 350°C), respectively. The magnetic contribution of Fe-based bcc structures comes mainly from the first NN environments and the total magnetic moment of iron can be assumed as being proportional to the weighted average of the hyperfine fields ($<B_{hf}>$) [39]. Thus, a rough estimation of the magnetic moment of all Fe-atoms in the α'-martensite is proportional to $\langle B_{hf} \rangle = \sum \frac{A^{Fe^i}}{\sum A^{Fe^i}} \cdot B_{hf}^{Fe^i}$, where "$i$" varies from 1 to 8 for the sextets displayed in Fig. 7. The values of $<B_{hf}>$ for the steel deformed to 80 % and annealed (30 min at 350°C) are 25.7 and 25.9 T, respectively.

For the steel annealed at 350 °C for 30 min, the five sextets are grouped into only three components (viz. Fe^8, Fe^7, Fe^1) and the sites with seven Fe NN (Fe^7) are split into three variants (viz. Fe^7_1, Fe^7_2 and Fe^7_3) with different values of isomer shift and quadrupole splitting (Fig. 7 and Table 2), suggesting that the one non-iron NN should be different in these variants although their hyperfine fields varies very little (viz. $B_{hf}^{Fe^7_1} = 27.9\ T$, $B_{hf}^{Fe^7_2} = 27.3\ T$, and $B_{hf}^{Fe^7_3} = 27.1\ T$, respectively). Results from Mössbauer spectroscopy also show that the sites with six (Fe^6) and four Fe-atoms as first nearest neighbors (Fe^4) are negligible after 30 min of annealing (Table 2). Yet, when comparing the area of each sextet (A^{Fe^i}) in the annealed specimen with the corresponding ones in the 80 % deformed state, the areas of the components Fe^8 decrease after annealing, whereas the others (Fe^7 and Fe^1) increase. These results strongly evidence the occurrence of selective short-range redistribution of atoms during short annealing times up to 30 min.

Table 2
Values of hyperfine field ($B_{hf}^{Fe^i}$), isomer shift (δ), quadrupole splitting (2ε) and relative area (A^{Fe^i}) for each sextet ($Fe^{\,i}$) and singlet, obtained from Fig. 6 for the steel deformed to 80% and for the corresponding specimen isothermally annealed at 350°C for 30 min. The superscript "i" varies from 8 to 1, denoting the number of Fe-ions as first neighbors in the respective subspectra.

Steel deformed to 80%

	Fe^8	Fe^7	Fe^6	Fe^4	Fe^1	Singlet
δ (mm/s) ±0.01	0.08	−0.16	0.11	0.03	0.02	−0.09
2ε (mm/s) ±0.01	0.23	−0.43	0.20	−0.02	−0.04	
$B_{hf}^{Fe^i}$ (T) ±0.1	28.7	27.5	26.2	22.7	18.1	
A^{Fe^i} (%) ±0.5	23.2	20.8	19.6	7.5	13.1	15.8

Steel deformed to 80 % and annealed at 350°C (30 min)

	Fe^8	Fe^7_1	Fe^7_2	Fe^7_3	Fe^1	Singlet
δ (mm/s) ±0.01	0.05	−0.30	0.65	0.13	−0.66	−0.09
2ε (mm/s) ±0.01	0.07	−0.57	0.33	−0.04	0.70	
$B_{hf}^{Fe^i}$ (T) ±0.1	29.8	27.9	27.3	27.1	16.2	
A^{Fe^i} (%) ±0.5	20.3	17.4	8.3	29.8	17.0	7.2

3.7. *Atom probe tomography*

The observations of long-range elemental partitioning in Fe-Mn alloys annealed for long periods of time at relative low temperatures [40, 41] lead us to associate this scenario with the changes in the values of M_s during stages 3 and 4 (Fig. 4a). Thus, the investigation of compositional partitioning effects in the studied steel was performed via atom probe tomography (APT). To ensure a homogenous extraction of regions containing only α'-martensite, we conducted APT measurements only for the specimens taken from the steel deformed to 80 % and subsequently annealed at 350°C (60 and 120 min).

Fig. 8a shows the three-dimensional reconstruction of an APT needle of the specimen deformed to 80 % and annealed at 350 °C for 60 min. In this figure, iso-composition surfaces for Mn (yellow) are constructed with a threshold value of 19 at. % and reveal the existence of Mn-segregation to lattice defects. The heterogeneous formation of Ni-enriched clusters is evidenced by means of iso-compositions surfaces (green) with a 5 at. % threshold, as pointed out by the red frame in the enlarged view given in Fig. 8a and b. We probed the composition along of a cluster of 7.5 nm as indicated by cylinder 1 of Fig. 8b. The obtained chemical profile is shown in Fig. 8c and it reveals that such nanodomains have a maximum of 5 at. % Ni and Al. The other elements contained in such cluster are predominantly Fe and Mn. For the sake of comparison, a second chemical profile was collected along the cylinder 2 (Fig. 8b) for a region devoid of Ni-enriched cluster and the obtained results are depicted in Fig. 8d. This figure evidences that the concentration of Mn segregated at the crystallographic defects can reach up to 28 at. %.

From the reconstruction specimen depicted in Fig. 8a, a region-of-interest was selected and extracted, as shown in Fig. 9a. Two-dimensional composition maps were extracted from the representative region highlighted by the green square with dimensions of 25 × 25 nm^2 in Fig. 9a. In such area, the Mn-segregated surface indicated by the white arrow was used as a reference for this analysis. The compositional distribution in terms of Mn, Si, Fe, Ni and Al is displayed in the maps depicted in Fig. 9b-f, respectively. Fig. 9 shows that chemical fluctuations are evident along the microstructure so that elemental segregation to defects seems to trigger spinodal-like decompositions as already demonstrated in binary Fe-Mn alloys annealed at low temperatures [41, 42]. In fact, the chemical composition on these defects reaches values as high as 30 at. % Mn and 6.3 at. % Si, indicating that these elements co-segregate jointly to lattice defects. Consequently, adjacent solute-depleted regions are formed displaying compositions of 9 at. % Mn and 1.5 at. % Si. Ni and Al are homogenously distributed within the microstructure independently on the presence of lattice defects.

The three-dimensional reconstruction of the APT specimen obtained from the steel deformed to 80 % and annealed at 350 °C for 120 min is shown in Fig. 10a. In this figure, Mn-segregation is highlighted by the iso-composition surfaces (golden) with a threshold value of 19 at. % Mn. For this annealing condition, the volume occupied by Mn-enriched zones is larger than that in the specimen annealed for 60 min (Fig. 8a). To better evaluate the long-range chemical partitioning in the specimen, the volume delimited by the blue box in Fig. 10a was used as a reference (Fig.10b) for extracting two-dimensional composition maps, which are reproduced in Fig. 10c-e for Mn, Si, Fe, Ni and Al, respectively. In Fig. 10c and d, the co-segregation of Mn and Si on the defects reach compositions as high as 33 at. % and 7.5 at. %, respectively. This

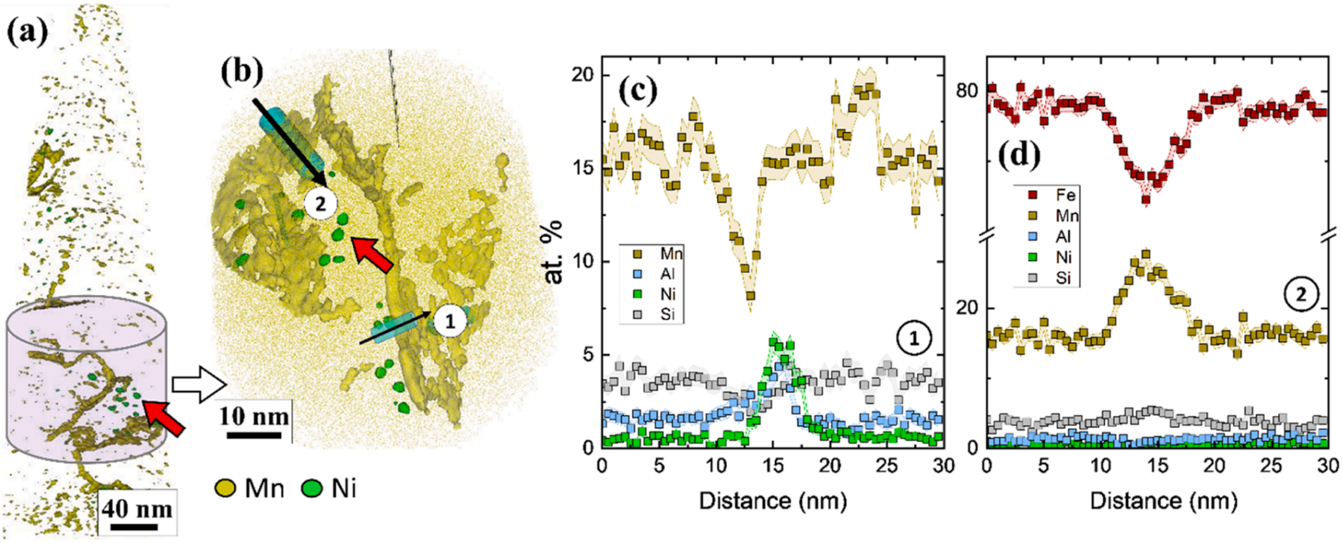

Fig. 8. Atom probe tomography (APT) measurements for the steel deformed to 80 % and isothermally annealed at 350 °C for 60 min. **(a)** Three-dimensional reconstruction of the specimen. Iso-compositions surfaces for Mn (yellow) are revealed with the threshold value of 19 at. % of Mn. Iso-compositions for Ni (green) are constructed using 5 at. % as a threshold value. **(b)** Enlarged view of the volume confined by the cylinder in (a). The red arrow highlights the presence of Ni-enriched nano-precipitates. (c) 1D chemical composition profile along Ni-rich nanoparticles in the region of interest identified by arrow number 1 in (b). Note the enrichment of both Ni and Al. (d) 1D chemical composition profile in a Mn-enriched lattice defect marked by arrow number 2 in (b), reaching 28 at. %Mn. (For interpretation of the references to color in this figure legend, the reader is referred to the web version of this article.)

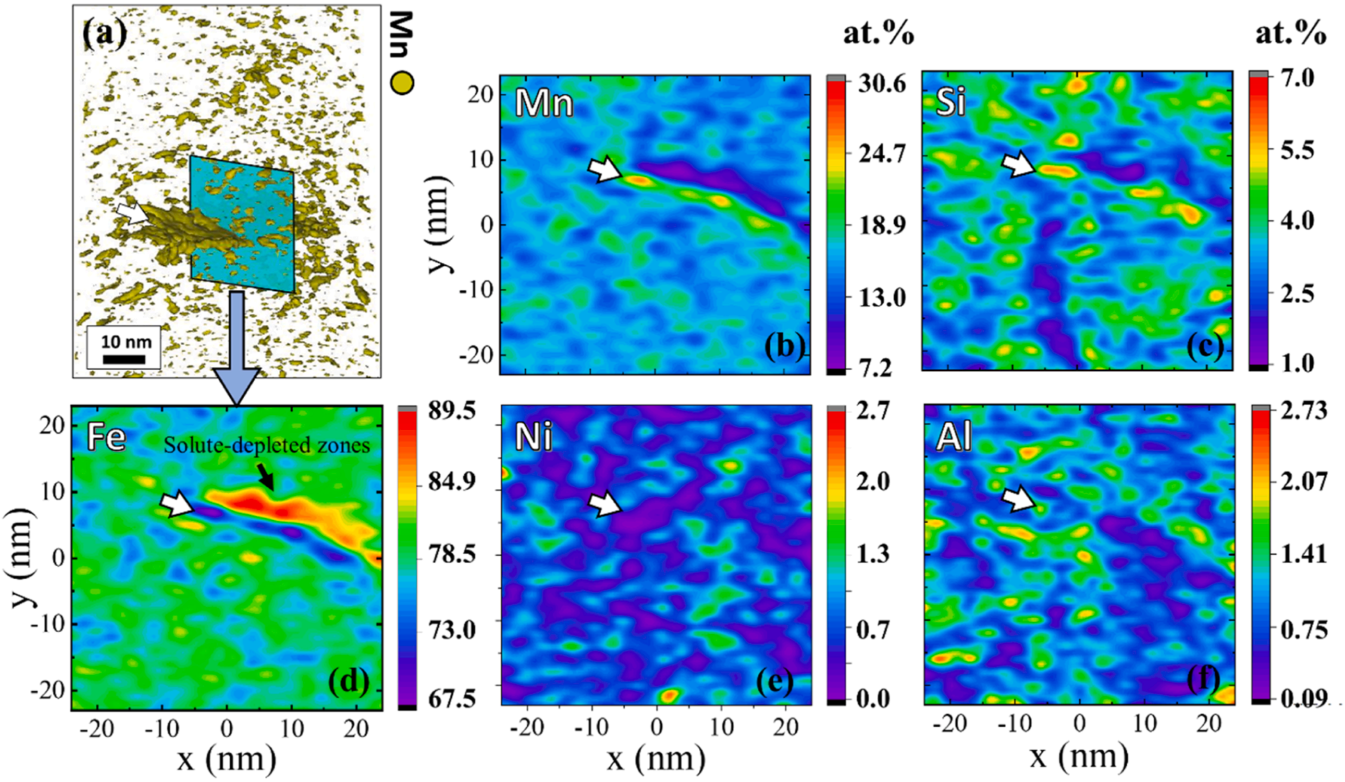

Fig. 9. Atom probe tomography (APT) measurements for the specimen deformed to 80 % and isothermally annealed at 350 °C for 60 min. **(a)** Partial reproduction of the three-dimensional reconstruction displayed in Fig. 8a. Two-dimensional composition maps in terms of **(b)** Mn, **(c)** Si, **(d)** Fe, **(e)** Ni and **(f)** Al, acquired from area delimitated by the green square of 25 × 25 nm^2 in (a). The white arrows indicate the projection of the segregated defect shown in (a), adopted as reference for this analysis. (For interpretation of the references to color in this figure legend, the reader is referred to the web version of this article.)

means that Fe depletion as low as 67 wt. % are expected within these zones. The chemical fluctuations in terms of Ni seems to be subtle, and no clear evidences of Ni-enriched clusters were readily obtained in Fig. 10a.

3.8. *The role of C: thermodynamic assessment and APT measurements*

In the Introduction, we quoted the hypothesis in which carbides ($M_{23}C_6$) precipitates at the austenite grain boundaries of some austenitic

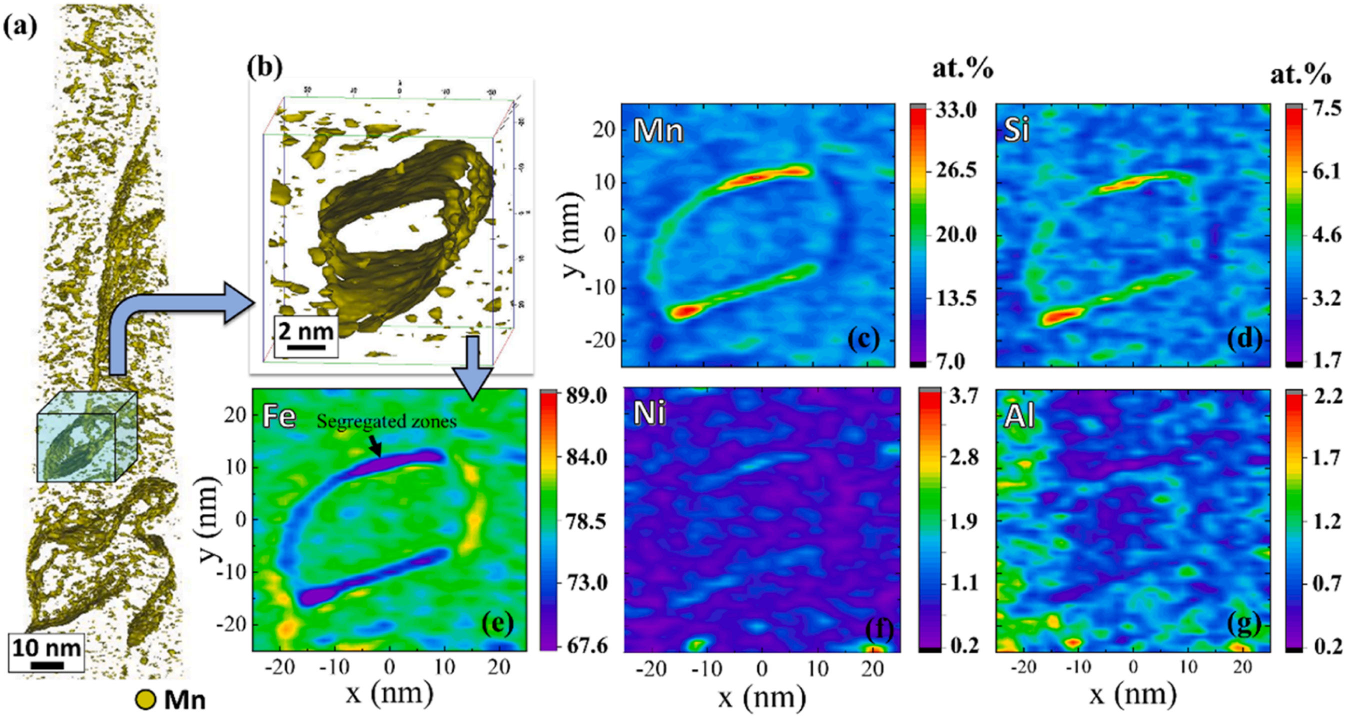

Fig. 10. Atom probe tomography (APT) measurements for the specimen deformed to 80 % and isothermally annealed at 350 °C for 120 min. **(a)** Three-dimensional reconstruction of the APT specimen. Iso-composition surfaces for Mn (yellow) are revealed using a threshold value of 19 at. %. **(b)** The box highlights the defect decorated with Mn-segregation chosen for this analysis. Two-dimensional composition maps in terms of **(c)** Mn, **(d)** Si, **(e)** Fe, **(f)** Ni and **(g)** Al, acquired from the cross-section of the tube displayed in (a). (For interpretation of the references to color in this figure legend, the reader is referred to the web version of this article.)

steels, thus depleting its surroundings in C, a fact that leads to an increase of the *martensite starting temperature* of the regions near such carbides. This fact, thus, consequently leads to the formation of additional α′-martensite formation upon cooling. In our study, we have sample variants (80 % deformed) which are fully depleted of austenite. Therefore, the likely precipitation of carbides could only occur within the bcc α′-martensite. To study comprehensively the possible formation of carbide in our material, we conducted thermodynamic calculations with the aid of the software ThermoCalc coupled with the data base TCFE9, as described in Section 2.7.

Fig. 11 shows the equilibrium phases expected for the investigated steel. For temperatures below 400°C, bcc α′-martensite can partially transform into either α-Mn or β-Mn together with a minute amount of $Ni_{0.48}Mn_{0.16}Al_{0.34}Fe_{0.02}$ (2 wt. %) and a very negligible percentage of 0.2 wt. % of $M_{23}C_6$ carbides (where M is Fe and/or Mn). Particularly at 350°C, the equilibrium quantities of $Ni_{0.48}Mn_{0.16}Al_{0.34}Fe_{0.02}$ and $M_{23}C_6$ are only ~0.67 % and ~0.16 %, respectively. Fig. 11 also shows that the austenite reversion is expected to start at 310°C, contrasting with the experimental temperature of 375 °C documented in Fig. 2. Besides, we did not observe the formation of β-Mn in our steel [43] and the 5 % Ni-containing nano-domains observed via APT (Fig. 8) are more likely an isolate formation of a local coherent constituent that seems to precede the precipitation of $Ni_{0.48}Mn_{0.16}Al_{0.34}Fe_{0.02}$. These discrepancies evidence that the investigated samples are not in equilibrium, thus allowing us to infer that, even under ideal conditions, the amount of $M_{23}C_6$ carbides to supposedly form in the investigated steel is very negligible, and its experimental detection could be extremely challenging if this constituent is not homogenously distributed within the microstructure.

To observe the spatial distribution of C within the microstructure, we further investigated the APT data collected for the material deformed to 80 % and annealed at 350 °C for 1 h, Fig. 12. The APT reconstruction shown in Fig. 12a evidences that C segregates at the crystallographic defects (in part, together with Mn) rather than precipitates as $M_{23}C_6$. A detailed inspection given by the two-dimensional elemental maps for C and Mn (Fig. 12b and c, respectively) help identify that the C concentration at such defects can be as high as 0.5 at. %, i.e., one order magnitude higher than the global C content of the steel (viz., 0.045 %C), Fig. 12b. In all regions evaluated in this specimen, the co-segregation of

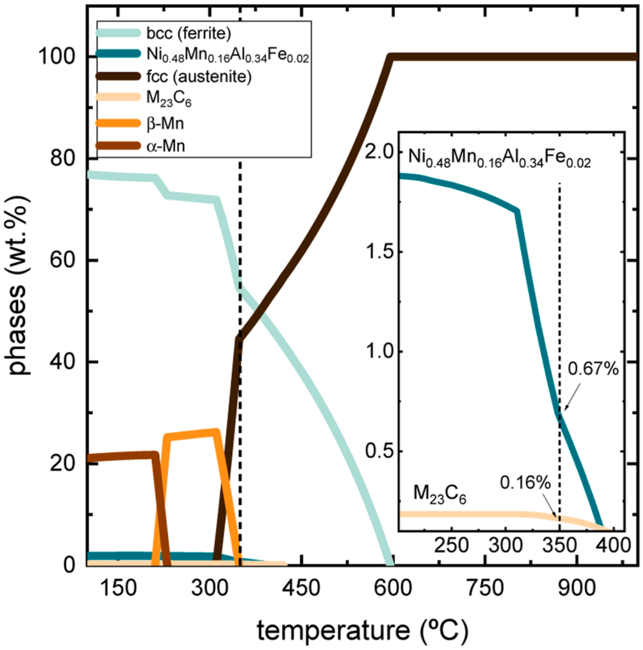

Fig. 11. Equilibrium phases as a function of temperature expected for the high-Mn TRIP steel. Results obtained with the aid of software ThermoCalc. (For interpretation of the references to color in this figure legend, the reader is referred to the web version of this article.)

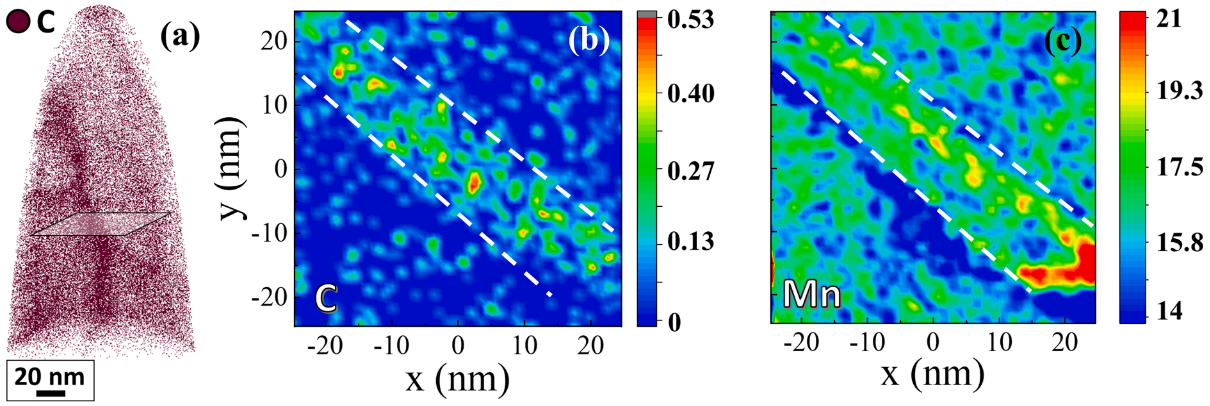

Fig. 12. Atom probe tomography (APT) measurements for the specimen deformed to 80 % and isothermally annealed at 350 °C for 60 min. (a) Three-dimensional reconstruction of the APT specimen. Two-dimensional composition maps in terms of (b) C and (c) Mn acquired from the cross-section displayed in (a). (For interpretation of the references to color in this figure legend, the reader is referred to the web version of this article.)

Mn and C does not reach the Mn(Fe):C atomic ratio of 80:20, ideally expected for the $M_{23}C_6$. Thus, we can infer that the local chemical fluctuations of Mn and C might similarly impact the magnetization of the material over stages 3 and 4 (Fig. 4a).

4. Discussion

For a cold-rolled high-Mn TRIP steel (16.8 wt %Mn) (Fig. 1), we investigated the underlying mechanisms of an anomalous increase of magnetization at 350°C (Figs. 2–4), which precedes the austenite reversion (α' →γ) in this material. At this point it is important to mention an anomalous magnetization behavior for $Co_3Sn_2S_2$ single crystal, recently reported by Shen et al. [44]. It is about an anomalous increase in magnetization which occurs for this material in a specific temperature range under cooling, upon low applied magnetic field. Such anomaly disappears for high applied fields, where the magnetization is saturated, and then was attributed to the depinning of magnetic domain walls [44]. In the present study, an anomalous increase of magnetization is seen from both in-situ (under heating) and ex-situ magnetic measurements (at the complete magnetization of the material) for the investigated material. Such anomaly is mirrored in its M_s behavior (taken at room temperature), for the samples isothermally annealed at 350°C (please, see Fig. 4). For such temperature, the material also presents an anomalous increase in magnetization under heating (please, see Fig. 2). Such features suggest that the anomalous magnetic behavior focused in this work has a different origin than what is reported in ref. [44].

Phase quantification performed by means of high-resolution XRD measurements (Fig. 5) and EBSD maps (Fig. 6) confirmed the absence of newly-fresh α'-martensite domains formed in high-Mn TRIP steel during annealing at 350°C (from 5 to 120 min). Such findings leaded us to rule out the premise 'anomalous coarsening of the α'-martensite domains, triggered by stress relief in the neighboring austenite' reported in Ref. [20] as the main explanation for the increase in magnetization of the studied steel (Fig. 3). Concerning the M_s behavior of the material annealed at 350°C for durations from 5 to 120 min (Fig. 4), we identified four stages, which will be discussed in the following:

4.1. Stage 1

The martensitic transformation in metastable paramagnetic austenite is accompanied by lattice distortion and creation of strong internal stress fields. Therefore, the influence of magneto-elastic effects on the magnetic properties cannot be neglected in studies of Fe-Mn alloys containing the ferromagnetic α'-phase [13–15]. The sensitivity of the magnetization in relation to external and internal stresses is known as Villari effect [15] and was recently demonstrated by Callahan et al. [13] to directly affect the saturation magnetization of medium-Mn TRIP steels, influencing thus the use of such parameter as tool for phase quantification. In the present case, the modified Williamson-Hall method (Fig. 5) confirmed that recovery takes place in the α'-martensite already in the early beginning of stage 1 through, whereas it is practically absent in the austenite. Therefore, the sharp increase of M_s after 5-min annealing is caused by stress relief in the α'-martensite (Villari effect) achieved through the annihilation of screw dislocations by cross-slip and dislocation climb [45,46].

4.2. Stage 2

The results obtained via Mössbauer spectroscopy (Fig. 7, Table 2) revealed a significant decrease of the relative area of the subspectrum (singlet) correspondent to paramagnetic phase (*i.e.*, austenite). The area of the subspectrum is proportional to the number of Fe-atoms present in each phase. In a preceding study, for a high-Mn steel with similar chemical composition, thermo-kinetic simulations combined with APT measurements revealed that Mn preferentially partitions to austenite over annealing treatments at ~ 400°C [26]. In other words, the fraction of Fe decreases in austenite as it gets enriched in Mn. Therefore, such change in composition can explain the observed change in the relative area of the singlet documented in Table 2.

Short-range chemical ordering promotes the rearrangement of a disordered random solid-solution bcc structure into B_2 or $D0_3$-ordered ones in several systems, including Fe-Al [37,47], Fe-Si [39,47-50] binary and Fe-Al-Si-Ni [51] quaternary ones. Such types of configurational structures are reported to decrease the magnetization as documented in ref. [37]. Due to the complex chemical composition of the studied steel and from the results displayed in Fig. 7 (Table 2) it is practically impossible to sort out precisely the nature of the ordered structures formed after 30-min annealing at 350 °C (stage 2). However, Table 2 indeed reveals that short-range solute redistribution occurred in the α'-martensite lattice during stage 2, creating different localized chemical configurations in terms of site occupancies for the Fe-ions and their corresponding nearest neighbors. The weighted average hyperfine fields ($<B_{hf}>$) calculated for both, the deformed (80 %) and annealed (30 min at 350 °C) specimens resulted in similar values, suggesting that their bulk magnetization are practically the same. The direct comparison of these $<B_{hf}>$ values is enabled by the fact that they consider all Fe-ions present in the α'-martensite, resulting in normalized values. This observation agrees well with the trend displayed by the values of M_s in Fig. 4, where M_s for the deformed and 30-min-annealed specimens present nearly the same values. This allows us to conclude that the selective short-range solute redistribution occurring with 30 min of annealing (stage 2) is the underlying mechanism for dropping the value of M_s in relation to those found in stage 1.

4.3. Stages 3 and 4

APT measurements enabled us to visualize long-range chemical fluctuations within the specimens exposed to longer annealing periods at 350 °C (60 and 120 min), as displayed in Figs. 8–10. During stage 3 (60 min), Mn, Si, and C segregate to the crystallographic defects of the samples, such as dislocations and interfaces (low-, high-angle boundaries) as already reported in the literature [52,53], thus promoting the creation of solute-depleted zones which are enriched in Fe and thus possess a higher magnetic signal. It is important to clarify that the nature of such crystallographic defects cannot be determined unequivocally through the APT dataset displayed in Figs. 8–10. The formation of local zones with high magnetic contribution along the entire specimen is hence attributed to increase the M_s values (Fig. 4) after annealing for 60 min. Extending the annealing time to 120 min, the segregated zones become slightly enriched in Mn and Si [41,42], but this fact does not significantly alter the absolute value of M_s – i.e., M_s during this stage remains nearly constant (as observed before in Fig. 4a). In the context of long-range chemical partitioning, spinodal-like decompositions were observed to cause changes in the Curie temperature [2] and coercivity [1] of ferromagnetic alloys, including permanent magnets [4]. In the present work, the results obtained from stages 3 and 4, however, shed light on the effect of spinodal decomposition triggered by elemental segregation on the magnetic signal, even before leading to the nucleation of fresh austenite (triggering the austenite reversion).

5. Summary and conclusions

A systematic investigation was carried out to reveal the underlying mechanisms responsible for increasing the values of M_s in a high-Mn steel deformed to 20 and 80 % of rolling. For isothermal conditions of annealing at 350 °C, XRD analysis and high-resolution microstructural characterization revealed the absence of further growth of α'-martensite. Short annealing treatments up to 15 min promoted the increase of M_s due to stress relief in α'-martensite. Further annealing to 30 min promotes the decrease in M_s driven by short-range ordering reactions. Finally, chemical fluctuations are observed after longer exposure times at 350 °C. As a consequence, the segregation of solutes to lattice defects enriches the matrix in Fe-content promoting the increase in M_s after 60 min. Further segregation occurs during 120 min but a raise in number of the zones with low magnetic contributions makes M_s decrease as well. The combinatorial magnetic and microstructural investigation reported here are important to clarify how local chemical changes and internal stresses are also directly associated with the magnetization of ferromagnetic Fe-based alloys. Our findings also shed new insights on the nature of the 'anomalous' magnetization, a phenomenon very often observed in TRIP steels, and how the associated local metallurgical changes impact the use of the saturation magnetization (M_s) as a reliable characterization tool for phase quantification.

CRediT authorship contribution statement

Maria J.R. Sandim: Formal analysis, Investigation, Writing – original draft. **Luiz C.C.M. Nagamine:** Formal analysis, Investigation, Writing – review & editing. **Alisson Kwiatkowski da Silva:** Investigation, Formal analysis. **Leonardo S. Aota:** Formal analysis, Writing – review & editing. **Liuliu Han:** Formal analysis, Investigation. **Renato Cohen:** Investigation, Writing – review & editing. **Hugo R.Z. Sandim:** Writing – review & editing, Formal analysis. **Baptiste Gault:** Writing – review & editing, Formal analysis. **Isnaldi R. Souza Filho:** Conceptualization, Formal analysis, Investigation, Writing – review & editing.

Declaration of competing interest

The authors declare that they have no known competing financial interests or personal relationships that could have appeared to influence the work reported in this paper.

Acknowledgments

The authors are grateful to Prof. Dr. D. B. dos Santos (DEMET-UFMG) for kindly supplying the steel used in this investigation. The authors are also grateful to U. Tezins and A. Sturm for their technical support with the atom probe tomography and focused ion beam facilities at the Max-Planck-Institut für Eisenforschung. B. Breitbach is also deeply acknowledged for the support with the XRD measurements. IRSF thanks to FAPESP (Sao Paulo Research Foundation, grant numbers: 2015/26409-8 and 2017/17170-7) for his scholarships. HRZS is CNPq Fellow (National Council for Scientific and Technological Development, Brazil) under Grant no. 308.296/2021-4.

Supplementary materials

Supplementary material associated with this article can be found, in the online version, at doi:10.1016/j.actamat.2024.119956.

References

[1] L. Zhou, W. Guo, J.D. Poplawsky, L. Ke, W. Tang, I.E. Anderson, M.J. Kramer, On spinodal decomposition in alnico - A transmission electron microscopy and atom probe tomography study, Acta Mater 153 (2018) 15–22.
[2] E.P. Butler, G. Thomas, Structure and properties of spinodally decomposed Cu-Ni-Fe alloys, Acta Metall. 18 (1970) 347–365.
[3] I. Joffe, P. Gaunt, Magnetic hardening and phase segregation in CuNiFe and CuNiCo alloys, J. Phys. D 4 (1971) 586–592.
[4] T.S. Chin, T.S. Wu, C.Y. Chang, Spinodal decomposition and magnetic properties of Fe-Cr-12Co permanent magnet alloys, J. Appl. Phys. 54 (1983) 4502–4511.
[5] D. Palanisamy, D. Raabe, B. Gault, On the compositional partitioning during phase transformation in a binary ferromagnetic MnAl alloy, Acta Mater. 174 (2019) 227–236.
[6] L. Bracke, L. Kestens, J. Penning, Transformation mechanism of α′-martensite in an austenitic Fe-Mn-C-N alloy, Scr. Mater. 57 (2007) 385–388.
[7] S. Allain, J.P. Chateau, O. Bouaziz, S. Migot, N. Guelton, Correlations between the calculated stacking fault energy and the plasticity mechanisms in Fe-Mn-C alloys, Mater. Sci. Eng. A 387-389 (2004) 158–162.
[8] L. Remy, A. Pineau, Twinning and strain-induced F.C.C. → H.C.P. transformation in the Fe-Mn-Cr-C system, Mater. Sci. Eng. 28 (1977) 99–107.
[9] G. Olson, M. Cohen, A mechanism for the strain-induced nucleation of martensitic transformations, J. Less-Common Met. 28 (1972) 107–118.
[10] G.B. Olson, M. Cohen, A general mechanism of martensitic nucleation: Part II. FCC → BCC and other martensitic transformations, Metall. Trans. A 7 (1976) 1905–1914.
[11] G.B. Olson, M. Cohen, A general mechanism of martensitic nucleation: Part I. General concepts and the FCC → HCP transformation, Metall. Trans. A 7 (1976) 1897–1904.
[12] H. Fujita, S. Ueda, Stacking faults and f.c.c. (γ) → h.c.p. (ϵ) transformation in 188 -type stainless steel, Acta Metall. 20 (1972) 759–767.
[13] M. Callahan, O. Hubert, F. Hild, A. Perlade, J.H. Schmitt, Coincidence of strain induced TRIP and propagative PLC bands in medium Mn steels, Mat. Sci. Eng. A 704 (2017) 391–400.
[14] O. Hubert, S. Lazreg, Two phase modeling of the influence of plastic strain on the magnetic and magnetostrictive behaviors of ferromagnetic materials, J. Magn. Magn. Mater. 424 (2017) 421–442.
[15] B.D. Cullity, C.D. Graham, Introduction to Magnetic Materials, 2nd ed., John Wiley and Sons, New Jersey, 2009.
[16] K.B. Guy, E.P. Butler, D.R.F. West, Reversion of bcc α′ martensite in Fe–Cr–Ni austenitic stainless steels, Met. Sci. 17 (1983) 167–176.
[17] R. Montanari, Increase of martensite content in cold rolled AISI 304 steel produced by annealing at 400°C, Mater. Lett. 10 (1990) 57–61.
[18] F. Gauzzi, R. Montanari, G. Principi, A. Perin, M.E. Tata, Martensite formation during heat treatments of AISI 304 steel with biphasic structure, Mat. Sci. Eng. A 273-275 (1999) 443–447.
[19] F. Gauzzi, R. Montanari, G. Principi, M.E. Tata, AISI 304 steel: anomalous evolution of martensitic phase following heat treatments at 400°C, Mat. Sci. Eng. A 438-440 (2006) 202–206.
[20] P.L. Mangonon, G. Thomas, The martensite phases in 304 stainless steel, Metall. Trans. 1 (1970) 1577–1586.
[21] A.F. Padilha, R.L. Plaut, P.R. Rios, Annealing of cold-worked austenitic stainless steels, ISIJ Int. 43 (2003) 135–143.

[22] M.J.R. Sandim, V. Mauro, S.S.M. Tavares, K.D. Zilnyk, H.R.Z. Sandim, Magnetic properties and microstructural characterization of cold-rolled and annealed 317L austenitic stainless steel, J. Magn. Magn. Mater. 539 (2021) 168336.
[23] M.J.R. Sandim, I.R. Souza Filho, C.F.G.S. Mota, K.D. Zilnyk, H.R.Z. Sandim, Microstructural and magnetic characterization of a lean duplex steel: strain-induced martensite formation and austenite reversion, J. Magn. Magn. Mater. 517 (2021) 167370.
[24] C.K. Mukhopadhyay, T. Jayakumar, R.V. Kasiviswanathan, B. Raj, Study of ageing-induced α'-martensite formation in cold-worked AISI type 304 stainless steel using an acoustic emission technique, J. Mater. Sci. 30 (1995) 4556–4560.
[25] I.R. Souza Filho, M.J.R. Sandim, R. Cohen, L.C.C.M. Nagamine, H.R.Z. Sandim, D. Raabe, Magnetic properties of a 17.6 Mn-TRIP steel: study of strain-induced martensite formation, austenite reversion, and athermal α′-formation, J. Magn. Magn. Mater. 473 (2019) 109–118.
[26] I.R. Souza Filho, A. Kwiatkowski da Silva, M.J.R. Sandim, D. Ponge, B. Gault, H.R. Z. Sandim, D. Raabe, Martensite to austenite reversion in a high-Mn steel: partitioning dependent two-stage kinetics revealed by atom probe tomography, in-situ magnetic measurements and simulation, Acta Mater. 166 (2019) 178–191.
[27] C. Gauss, I.R. Souza Filho, M.J.R. Sandim, P.A. Suzuki, A.J. Ramirez, H.R. Z. Sandim, In situ synchrotron X-ray evaluation of strain-induced martensite in AISI 201 austenitic stainless steel during tensile testing, Mat. Sci. Eng. A 651 (2016) 507–516.
[28] I.R. Souza Filho, M.J.R. Sandim, D. Ponge, H.R.Z. Sandim, D. Raabe, Strain hardening mechanisms during cold rolling of a high-Mn steel: interplay between submicron defects and microtexture, Mat. Sci. Eng. A 754 (2019) 636–649.
[29] I.R. Souza Filho, D.R. Almeida Junior, C. Gauss, M.J.R. Sandim, P.A. Suzuki, H.R. Z. Sandim, Austenite reversion in AISI 201 austenitic stainless steel evaluated via in situ synchrotron X-ray diffraction during slow continuous annealing, Mat. Sci. Eng. A 755 (2019) 267–277.
[30] A.K De, J.G. Speer, D.K. Matlock, D.C. Murdock, M.C. Mataya, R.J. Comstock, Deformation-induced phase transformation and strain hardening in type 304 austenitic stainless steel, Metall. Mater. Trans. A 37 (2006) 1875–1886.
[31] T. Ungár, A. Borbély, The effect of dislocation contrast on x-ray line broadening: a new approach to line profile analysis, Appl. Phys. Lett. 69 (1996) 3173–3175.
[32] T. Ungár, I. Dragomir, Á. Révész, A. Borbély, The contrast factors of dislocations in cubic crystals: the dislocation model of strain anisotropy in practice, J. Appl. Crystallogr. 32 (1999) 992–1002.
[33] K. Thompson, D. Lawrence, D.J. Larson, J.D. Olson, T.F. Kelly, B. Gorman, In situ site-specific specimen preparation for atom probe tomography, Ultramicroscopy 107 (2007) 131–139.
[34] B.P. Geiser, D.J. Larson, E. Oltman, S. Gerstl, D. Reinhard, T.F. Kelly, T.J Prosa, Wide-field-of-view atom probe reconstruction, Microsc. Microanal. 15 (2009) 292–293.
[35] L. León-Reina, M. Garciá-Maté, G. Ávarez-Pinazo, I. Santacruz, O. Vallcorba, A. G. De La Torre, M.A.G. Aranda, Accuracy in Rietveld quantitative phase analysis: a comparative study of strictly monochromatic Mo and Cu radiations, J. Appl. Crystallogr. 49 (2016) 722–735.
[36] Y. Tomota, Y. Morioka, W. Nakagawara, Epsilon martensite to austenite reversion and related phenomena in Fe-24Mn and Fe-24Mn-6Si alloys, Acta Mater 46 (1998) 1419–1426.
[37] Q. Zeng, I. Baker, Magnetic properties and thermal ordering of mechanically alloyed Fe-40 at% Al, Intermetallics 14 (2006) 396–405.
[38] D.H Sherman, S.M Cross, S. Kim, F. Grandjean, G.J. Long, M.K. Miller, Characterization of the carbon and retained austenite distributions in martensitic medium carbon, high silicon steel, Metall. Mater. Trans. A 38 (2007) 1698–1711.
[39] J. Karel, J. Juraszek, J. Minar, C. Bordel, K.H. Stone, Y.N. Zhang, J. Hu, R.Q. Wu, H. Ebert, J.B. Kortright, F. Hellman, Effect of chemical order on the magnetic and electronic properties of epitaxial off-stoichiometry Fe_x-Si_{1-x} thin films, Phys. Rev. B 91 (2015) 144402.
[40] A. Kwiatkowski da Silva, G. Inden, A. Kumar, D. Ponge, B. Gault, D. Raabe, Competition between formation of carbides and reversed austenite during tempering of a medium-manganese steel studied by thermodynamic-kinetic simulations and atom probe tomography, Acta Mater. 147 (2018) 165–175.
[41] A. Kwiatkowski da Silva, D. Ponge, Z. Peng, G. Inden, Y. Lu, A. Breen, B. Gault, D. Raabe, Phase nucleation through confined spinodal fluctuations at crystal defects evidenced in Fe-Mn alloys, Nat. Commun. 9 (2018) 1137.
[42] A. Kwiatkowski da Silva, R.D. Kamachali, D. Ponge, B. Gault, J. Neugebauer, D. Raabe, Thermodynamics of grain boundary segregation, interfacial spinodal and their relevance for nucleation during solid-solid phase transitions, Acta Mater 168 (2019) 109–120.
[43] A. Kwiatkowski da Silva, I.R. Souza Filho, W. Lu, K.D. Zilnyk, M.F. Hupalo, L. M. Alves, D. Ponge, B. Gault, D. Raabe, A sustainable ultra-high strength Fe18Mn3Ti maraging steel through controlled solute segregation and α-Mn nanoprecipitation, Nat. Commun. 13 (2022) 2330.
[44] Z. Shen, X.D. Zhui, R.R. Ullah, P. Klavin, V. Taufour, Anomalous depinning of magnetic domain walls within the ferromagnetic phase of the weyl semimetal $Co_3Sn_2S_2$, J. Phys.: Condens. Matter 35 (2023) 045802.
[45] F.J. Humphreys, M. Hatherly, Recrystallization and Related Annealing Phenomena, 1st ed., Elsevier Science Ltd., Kidlington, 1995.
[46] D. Raabe, Recovery and recrystallization: phenomena, physics, models, simulation, in: D.E. Laughlin, K. Hono (Eds.), Physical Metallurgy, Elsevier, 2014, pp. 2291–2397.
[47] O.I. Gorbatov, Y.N. Gornostyrev, A.R. Kuznetsov, A.V. Ruban, Effect of magnetism on short-range order formation in Fe-Si and Fe-Al alloys, Solid State Phenom. 172-174 (2011) 618–623.
[48] G. Inden, The role of magnetism in the calculation of phase diagrams, Physica B 103 (1981) 82–100.
[49] G. Inden, The effect of continuous transformations on phase diagrams, Bull. Alloy Phase Diagr. 2 (1982) 412–422.
[50] N.V. Ershov, N.M. Kleĭnerman, V.A. Lukshina, V.P. Pilyugin, V.V. Serikov, Specific features of the local atomic structure of a Fe-Si alloy in the α area of the phase diagram, Phys. Solid State 51 (2009) 1236–1242.
[51] M. Miyazaki, M. Ichikawa, T. Komatsu, K. Matusita, Mossbauer effect study of ordering in Fe-Al-Si and Fe-AI-Si-Ni magnetic thin films, IEEE Trans. Magn. 28 (1992) 2430–2432.
[52] D. Raabe, S. Sandlöbes, J. Millán, D. Ponge, H. Assadi, M. Herbig, P.-P. Choi, Segregation engineering enables nanoscale martensite to austenite phase transformation at grain boundaries: a pathway to ductile martensite, Acta Mater. 61 (2013) 6132–6152.
[53] D. Raabe, M. Herbig, S. Sandlöbes, Y. Li, D. Tytko, M. Kuzmina, D. Ponge, P.-P. Choi, Grain boundary segregation engineering in metallic alloys: a pathway to the design of interfaces, Curr. Opin. Solid State Mater. Sci. 18 (2014) 253–261.